CONEM
CONGRESSO NACIONAL DE ENGENHARIA MECÂNICA
NATAL - RIO GRANDE DO NORTE - BRASIL

ABCM

XII CONGRESSO NACIONAL DE ENGENHARIA MECÂNICA
DE 29/07 A 02/08 DE 2024, NATAL-RN, BRASIL

CONEM2024-1469 ANALYSIS COMPARING THE PIERSON-MOSKOWITZ AND BRETSCHNEIDER SPECTRA FOR THE MORISON EQUATION

Davi Kauê de Sousa Gomes, davi.gomes@ufpi.edu.br[1]
Anderson Soares da Costa Azevêdo, anderson.sca@usp.br[2]
Simone dos Santos Hoefel, simone.santos@ufpi.edu.br[1]

[1]Universidade Federal do Piauí, Laboratório de Mecânica Computacional - LaMeC
[2]Universidade de São Paulo, Escola Politécnica da Universidade de São Paulo, São Paulo-SP Brasil

Abstract: *Most wind power is generated on onshore structures, but in the last ten years, offshore wind turbines have gained prominence due to their superior wind quality and abundance of space in the ocean environment. This increase in demand for offshore structures show the importance of understanding how these facilities respond to the maritime environment. Recent studies have focused on analyzing the impact of loads from wind, currents and waves, highlighting the need for a precise formulation for each component of these forces. This article focuses on the elaboration of the distributed transverse fluid load, employing the semi-empirical equation developed by Morison to model the in-plane fluid force. The out-of-plane force, exemplified by the shedding of vortices, is approached in a simplified way, taking the form of a sine wave. To achieve this objective, random waves are modeled by the Airy linear wave theory, incorporating both the Pierson-Moskowitz (P-M) spectrum, Bretschneider spectrum, while also applying the central limit theorem. The P-M spectrum consideres only one parameter, the wind velocity, which can be interpreted as the significant wave height, whereas the Bretschneider spectrum incorporates two parameters, additionally considering the duration of the wind. This approach not only enables the accurate reproduction of wave profiles in the spatial and temporal domains, but also allows the observation of striking surface effects in shallow waters, contrasting with the smoother profiles in deep waters. Is numerically demonstrated that the wave profile curve shifts for both spectra as a result of the newly added parameter. This methodology facilitates the assessment of wave speeds in relation to depth. The evaluation of the out-of-plane force revealed it to be insignificant in situations of low Reynolds numbers, but it becomes noticeable at high Reynolds numbers, leading to oscillation of the fluid close to the structure due to the vortices. Finally, improvements in predicting this oscillation aid in preventing natural frequencies synchronization with shed vortices that could lead to structural collapse.*

Keywords: *Morison's equation, Power Spectrum, offshore structures*

1. INTRODUCTION

A strategy for reducing carbon emissions in the global energy system involves the utilization of renewable energy sources. This, coupled with the plentiful occurrence of wind in ocean environments and the benefits of ample space, has made offshore wind turbines one of the most coveted energy sources. Onshore turbines still dominate the market, as highlighted by James and Ros (2015), due to the requirement for fixed offshore structures to be situated in relatively shallow water depths, a condition not universally met by every country. To overcome this, the technology advances into deeper waters, floating platforms and compliant structures has developed for wind turbines. This advancement also created the need to formulate more precise environmental loads (Wan *et al.*, 2017).

According to Silva (2007), the ocean environment introduces seven distinct types of forces that can act on a body. These include the drag force, which is necessary to maintain a body stationary in a fluid with constant velocity and the inertia force, required to keep a structure in a uniformly accelerating flow. Additionally, the added mass force is essential for accelerating a body submerged in a fluid, while diffraction occurs when incident waves scatter on the structure's surface. The Froude-Krylov force represents pressure exerted on the structure by incident waves, while the lift force denotes the perpendicular component of the flow. The wave slamming force, primarily occurring at the free surface, results from particularly high amplitude and energy waves.

To study these forces, three different theories are used to investigate wave forces in offshore structures: the Morison equation, the diffraction theory, and the Froude-Krylov theory (Sarpkaya, 2010). The application of each theory resides in the type and size of the structures. When the size is small compared with the wavelength, is used the Morison equation,

which assumes that the drag force component is predominant when compared to the inertia force component. While the inertia component predominates over the drag component, but the structure still small, the Froude-Krylov theory is applied. But, if the structure isn't small compared with the wavelength, the structure starts to change the wave field of the incident waves. This way the diffraction of the waves in the structure needs to be taken in account, so the diffraction theory must be used (Stansby *et al.*, 2017). In this study, the assumption will be made that the size of the structure is small compared to the wavelength, allowing for the application of the Morison equation. Additionally, a modified version of the original equation will be employed to account for the added mass force in compliant structures.

2. MORISON EQUATION

Morison *et al.* (1950) derived an equation for a stationary cylinder under a fluid force composed of two components: the inertia component that represents the fluid force when a water particle accelerates and decelerates as it passes through the structure and the drag component that occurs due to the difference of pressure between the downstream and the upstream flow region, and the drag force is proportional to the square of the water particle velocity.

The semi-empirical Morison equation is given by:

$$f^n = C_M \cdot m_{fl} \cdot \frac{\partial V_{rel}^n}{\partial t} + C_D \cdot r_o \cdot \rho_f \cdot V_{rel}^n \cdot |V_{rel}^n|, \tag{1}$$

in which f^n is the force per unit length of the cylinder, C_M is the inertia coefficient, C_D is the drag coefficient, r_o is the external radius of the cylinder, ρ_f is the density of the water, m_{fl} is the mass of displaced fluid per unit length, that can be written as $m_{fl} = r_o^2 \cdot \rho_f \cdot \pi$, and V_{rel}^n is the relative velocity normal to the structure element, and is written as:

$$V_{rel}^n = w^n + U_c^n - \dot{R}^n, \tag{2}$$

where w^n is the wave velocity, U_c^n is the current velocity that follows the flow direction as show in Fig. 1, and R^n is the position vector from the base to the study location. If is a fixed structure, the R^n value is equal to zero, and only w^n depends on time, so is possible to substitute the derivation in the inertia force parcel to $\dot{w}^n$ (Journée and Massie, 2001).

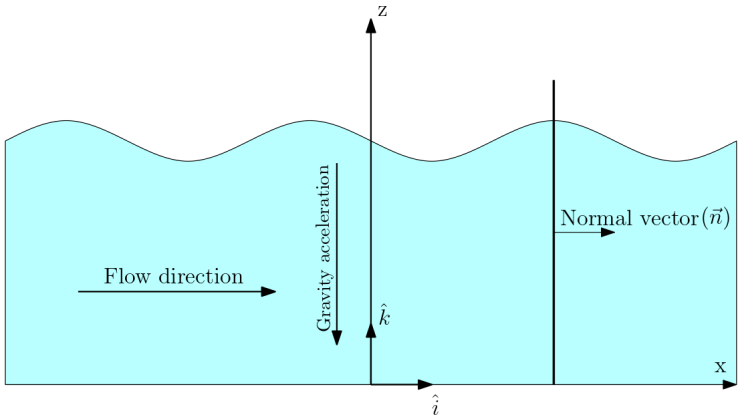

Figure 1: Fixed structure

Where $\hat{n}$ represents the normal vector perpendicular to the structure. By applying the coordinate system depicted in Fig. 1, the components constituting the relative velocity can be reformulated as:

$$\begin{aligned} \vec{w} &= \hat{i} \cdot w_x + \hat{k} \cdot w_z, \\ \vec{U_c} &= \hat{i} \cdot U_c, \\ \vec{R} &= \hat{i} \cdot u + \hat{k} \cdot v, \end{aligned} \tag{3}$$

where none of the velocities have y component. The wave velocities ($\vec{w}$) is decomposed in two components: w_x and w_z. Similar to the wave velocities, the position vector has two components: u for the deformation in x and v for the deformation in z (Han and Benaroya, 2002).

The terms inserted in Eq. (2) are orthogonal to the displacement of the structure, so from the vector analysis it is possible to rewrite these terms as a triple vector product as follows in:

$$\begin{aligned} w^n &= |\vec{t} \times \vec{w} \times \vec{t}|, \\ U_c^n &= |\vec{t} \times \vec{U_c} \times \vec{t}|, \\ R^n &= |\vec{t} \times \vec{R} \times \vec{t}|, \end{aligned} \tag{4}$$

in which $\vec{t}$ is the vector tangent to the structure displacement (Fang and Duan, 2014).

2.1 Modified Morison Equation

When modeling a compliant structure, i.e. structures that are designed to have small deformation, the equation derived by Morison has a small modification, including the added mass term. This represents the phenomenon that when a structure accelerates through a fluid medium, the fluid is also accelerated. The equation that represents the force to accelerate the structure, is represented by (Han and Benaroya, 2002):

$$F = (m_{str} + C_A \cdot m_{flu})\ddot{v}, \tag{5}$$

where m_{flu} is the mass of the displaced fluid, $\ddot{v}$ is the acceleration of the structure, and C_A is the added mass coefficient, that is related with C_M by:

$$C_A = C_M - 1. \tag{6}$$

Then, with the addition of the displaced fluid and applying the Newton notation to the derivatives, the Eq. (1) can be rewritten as:

$$f^n = C_M \cdot m_{fl} \cdot \dot{w}^n + C_D \cdot r_o \cdot \rho_f \cdot V_{rel}^n \cdot |V_{rel}^n| - C_A \cdot m_{fl} \cdot \ddot{R}^n, \tag{7}$$

the hydrodynamic resisting force opposes the direction of cylinder acceleration, as denoted by the minus sign in the last therm of the equation, as show in the Fig. 2, where F_{fl} represents this resisting force, opposed to the flow direction.

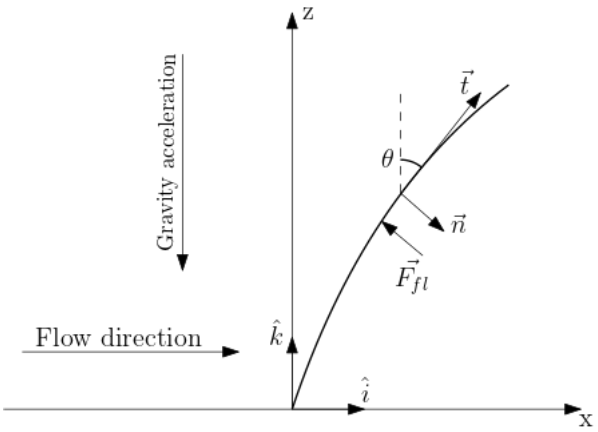

Figure 2: Compliant structure motion.

Considering that the angle of deflection is small, is possible to approach $sen\theta$ to u', this way the vector tangent to the structure with is represented by $\vec{t}$ is represented by $\vec{t} = \hat{k} + \hat{i} \cdot u'$. Similarly, as $\vec{t}$ it is possible to write the normal vector ($\vec{n}$) to the structure displacement, defined as $\vec{n} = -u' \cdot \hat{k} + \hat{i}$, with the normal vector it is possible to rewrite the relationship show in Eq. (4) as a dot product, the result of this is given as:

$$\begin{aligned} w^n &= \vec{n} \cdot \vec{w} = -u' \cdot w_z \cdot \hat{k} + w_x \cdot \hat{i}, \\ U_c^n &= \vec{n} \cdot \vec{U_c} = U_c \cdot \hat{i}, \\ R^n &= \vec{n} \cdot \vec{R} = -u' \cdot v \cdot \hat{k} + u \cdot \hat{i}, \end{aligned} \tag{8}$$

this way is possible to write the Eq. (2) as $V_{rel}^n = -w_z \cdot u' + \dot{v} \cdot u' + w_x + U_c - \dot{u}$, incorporating this sentence in the (Eq. 7), it is rewritten as:

$$\begin{aligned} f^n = {} & C_M \cdot m_{fl} \cdot (-w_z \cdot u' + w_x) \\ & + C_D \cdot r_o \cdot \rho_f \cdot (-w_z \cdot u' + \dot{v} \cdot u' + w_x + U_c - \dot{u}) \times | - w_z \cdot u' + \dot{v} \cdot u' + w_x + U_c - \dot{u}| \\ & - C_A \cdot m_{fl} \cdot (\ddot{v} \cdot u' + \ddot{u}). \end{aligned} \tag{9}$$

2.2 Fluid Coefficient

According to Wilson (2003) a fluid has three classical parameters: the inertia, added mass and drag coefficients. The interpretation of C_M and C_D can be gleaned by referring to Eq. (1), where C_M connects the force per unit length F needed to keep a rigid cylinder stationary in a fluid with a uniform and constant free stream acceleration of magnitude $\dot{w}^n$. C_D is associated with the force required to maintain a fully immersed cylinder when subjected to a constant free stream fluid velocity V_{rel}^n.

These coefficients necessitate experimental determination. However, for a long cylinder, C_M tends to approach its theoretical limit of 2 under conditions of uniformly accelerated flow. If the inertia coefficient approaches its limit value, simultaneously C_A approaches 1 by Eq. (6). For high Reynolds number, the drag coefficient also approaches 1. The added mass coefficient is related with the inertia coefficient as show by Eq. (6), and the last two parameters, inertia and drag coefficients, they depend on at least three other parameters:

$$\begin{aligned} C_M &= C_M(R_e, K_c, Cylinder\ roughness) \\ C_D &= C_D(R_e, K_c, Cylinder\ roughness), \end{aligned} \tag{10}$$

where R_e is the Reynolds number and K_c is the Keulegan-Carpenter number, both given by:

$$R_e = \frac{\rho_f \cdot U \cdot D}{\mu},\ K_c = \frac{U \cdot T}{D}. \tag{11}$$

where ρ_f is the density of the fluid, U is the free stream velocity, D is the outer diameter of the structure, μ is the dynamic or absolute viscosity, and T is the wave period (Benaroya and Han, 2005).

Defined by Keulegan and Carpenter (1958) the K_c is a dimensionless parameter that characterizes the significance of drag forces compared to inertia forces in the context of oscillatory fluid flow around structures. In scenarios with small Keulegan-Carpenter numbers, inertia prevails, whereas in cases with large numbers, drag forces become prominent (Mao *et al.*, 2018).

Similarly, the Reynolds number is also a dimensionless parameter used to predict how the flow regime pass through a structure, for small Reynolds number the flow separates and reunites smoothly, and as the number increases, the vortex street forms in closer proximity to the cylinder, eventually reaching a point where the attached eddies themselves initiate oscillations (Zauner *et al.*, 2018).

3. Ocean Waves Formulation

The drag exerted by the wind as it moves across the water's surface is responsible for generating the majority of steady large ocean currents, and they stay near the ocean surface. Tidal currents are created by gravitational forces, and their most pronounced effects occur near the coastlines. And the last current therm, the ocean circulation, is given by the radiation heating provided by the sun. With the combined flow field, it is possible to evaluate the wave loads when ocean waves and currents act at the same time in the structure. The interaction of waves and non-uniform currents causes a complex phenomenon, with will not be discussed in this work. For the uniform current, the relationship between current and wave is given by $V_{rel}^n = w^n + U_c^n \cdot cos(\beta)$, where β is the angle between the current and wave direction, with in this case will be considerate zero, so the equation return to Eq. (2) without the displacement vector (Nizamani *et al.*, 2019).

The current velocity magnitude (U_c^n) is evaluated using three different components: a tidal component (U_{tidal}), a low-frequency component associated with the circulation (U_{circ}) and a wind-induced drift current (U_{wind}). According to, Isaacson (1988) the empirical equation that relates all of these terms is given by:

$$U_c^n = (U_{tidal} + U_{circ}) \cdot \left(\frac{z_o + d}{d}\right)^{1/7} + U_{wind} \cdot \left(\frac{z_o + do}{do}\right), \tag{12}$$

where z_o is the seawater level vertical coordinate measured upwards from the still water level, d is the total depth of the water and do is the depth of the thermocline or 50m, whichever is less.

Each of the components for the current velocity magnitude are obtained in an empirical way, the tidal component is given by tide tables and the drift component is about 3% of the 10 minutes mean wind velocity at $10m$ above the sea level (Bar-Avi and Benaroya, 1997). It is important to highlight that the development of these currents occurs at a slow pace when compared to the timescale of engineering concerns. As a result, they can be considered a quasi-steady phenomenon. Conversely, waves cannot be regarded as a steady phenomenon because the intricate physics governing wave dynamics are too complex, necessitating a stochastic modeling approach (Besedin *et al.*, 2018).

Oceanographers and statisticians have determined that for engineering purposes, the surface elevation at a specific ocean location can be modeled as an ergodic process with a Gaussian distribution. This implies that a single sample taken for the wave surface elevation is sufficiently typical to represent the entire process. Consequently, an indicator delineating the repetitive nature or harmonic characteristics of the wave, along with its distribution, becomes essential. Which is achieved through the utilization of a Spectral density function (Hughes and Paik, 2010).

These wave spectra involve three distinct parameters: the wind speed (U_w), the duration of the wind (t), and the fetch (x) over which the wind blows. However, the spectrum can also be expressed in terms of: the significant wave height (H_s), which is the average height of the highest one-third of all waves; the peak time period (T_p), representing the time period with the highest spectral peak; and the peakedness factor (γ), which enhances the peak frequencies (Khedkar *et al.*, 2021). When analyzing a fully developed sea, which refers to a sea state where the wind blowing is independent of the duration of the wind and the fetch, it becomes possible to approximate the energy spectral distribution by applying the Pierson-Moskowitz spectrum (P-M spectrum), which is given as:

$$S_{\eta\eta}(\omega) = \alpha \cdot g^2 \cdot \omega^{-5} \cdot \exp\left(\frac{-1.25 \cdot \omega_p}{\omega}\right), \tag{13}$$

where α, known as Phillip's constant, is equal to 0.0081, and ω_p, denoting the peak frequency, is expressed as:

$$\omega_p = \left(\frac{0.161 \cdot g}{H_s}\right)^{1/2}, \tag{14}$$

this relationship between the peak frequency and the significant wave height is derived by setting the first derivative of Eq. (13) to zero (Prendergast *et al.*, 2020). In the case of a "nearly"developed sea, wherein the influence of time on the wave spectrum is evaluated, the P-M equation, characterized by only one parameter, gives way to the Bretschneider spectrum as a more fitting model. The Bretschneider spectrum, featuring two parameters, is expressed as follows:

$$S_{\eta\eta}(\omega) = \frac{5 \cdot \omega_p^4}{16 \cdot \omega^5} \cdot H_s^2 \cdot \exp\left(-\frac{5 \cdot \omega_p^4}{4 \cdot \omega^4}\right), \tag{15}$$

in this scenario, as the peak period serves as one of the parameters, Eq. (14) is reformulated as $\omega_p = \frac{2\pi}{T_p}$, if this peak period is applied to the Bretschneider's equation, it yields an equivalent value to that of a P-M spectrum (Sjolte *et al.*, 2013).

In order to obtain the velocities and accelerations exercised by waves, is used the Airy linear wave theory, with gives the description of gravity waves profile, and power spectral density to evaluate the wave height. An ocean wave can be represented, in a simple way, as a pure sinusoidal oscillation about the still water level. (Han and Benaroya, 2000).

Thus, the wave profile can be expressed as follows:

$$\eta(x,t) = \frac{H}{2} \cdot cos(k \cdot x - \omega \cdot t), \tag{16}$$

where $H/2$ is the amplitude, k is the wave number and ω is the angular frequency. The respective horizontal and vertical velocity components are given by:

$$\begin{aligned} w_y(x,z,t) &= \frac{H}{2} \cdot \omega \cdot \frac{cosh(k \cdot z)}{senh(k \cdot d)} \cdot cos(k \cdot y - \omega \cdot t), \\ w_x(x,z,t) &= \frac{H}{2} \cdot \omega \cdot \frac{senh(k \cdot z)}{senh(k \cdot d)} \cdot sen(k \cdot y - \omega \cdot t), \end{aligned} \tag{17}$$

unlike the wave profile, this equation is also contingent upon the total depth of the water (d) and the vertical ordinate measured from the bottom of the sea (x). Wherein the dispersion relationship between the wave number and angular frequency is (Mirab *et al.*, 2015):

$$\omega^2 = g \cdot k \cdot tanh(k \cdot d). \tag{18}$$

This approach fails to accurately replicate sea waves. Instead, it utilizes a superposition of numerous waves, each characterized by a random phase and distinct angular frequencies. This way $\eta(y,t)$ is expressed as follows:

$$\eta(x,t) = \sum_{n=1}^{N} cos(\bar{k}_n \cdot x - \bar{\omega}_n \cdot t - \varphi_n) \cdot \sqrt{2 \cdot \Delta\omega_n \cdot S_{\eta\eta}(\bar{\omega}_n)} \tag{19}$$

where $\bar{\omega}$ is the mean of the frequencies, $\bar{k}$ is the respective wave number of $\bar{\omega}$, given by Eq. (18), φ_n is a random number between 0 and 2π, $\Delta\omega_n$ is the different between the frequencies and $S_{\eta\eta}(\bar{\omega}_n)$ is the spectral density. Therefore, the respective wave velocities are given by:

$$w_x(x,z,t) = \sum_{n=1}^{N} \bar{\omega} \cdot \frac{cosh(\bar{k}\cdot z)}{senh(\bar{k}\cdot d)} \cdot cos(\bar{k}_n \cdot x - \bar{\omega}_n \cdot t - \varphi_n) \cdot \sqrt{2 \cdot \Delta\omega_n \cdot S_{\eta\eta}(\bar{\omega}_n)},$$
$$w_z(x,z,t) = \sum_{n=1}^{N} \bar{\omega} \cdot \frac{senh(\bar{k}\cdot z)}{senh(\bar{k}\cdot d)} \cdot sen(\bar{k}_n \cdot x - \bar{\omega}_n \cdot t - \varphi_n) \cdot \sqrt{2 \cdot \Delta\omega_n \cdot S_{\eta\eta}(\bar{\omega}_n)}. \quad (20)$$

and the expression $\sqrt{2 \cdot \Delta\omega_n \cdot S_{\eta\eta}(\bar{\omega}_n)}$ represent the amplitude of the wave (Ishiharaa and Zhang, 2018).

4. RESULTS

For the subsequent analysis, will be examined two distinct configurations of wave parameters to assess a comparison between them. These configurations differ by the T_p parameter, while the values for H_s and depth were proposed by Han and Benaroya (2002). The respective values for each configuration are presented in Tab. 1:

Table 1: Wave data.

Parameters	H_s	T_p	N	ω_N	depth
Wave 1	6.364 (m)	15.7654 (s)	15	1.5 (rad/s)	480 (m)
Wave 2	6.364 (m)	9.4592 (s)	15	1.5 (rad/s)	480 (m)

where N represents the number of superposed of Airy waves utilized in the irregular wave sample, and ω_N is selected to contain the majority of the energy spectrum. Since the Pierson-Moskowitz spectrum disregards the peak period, both waves exhibit similar responses. However, when contrasted with the Bretschneider spectrum, the curve shifts for both scenarios, as show in Fig. (4):

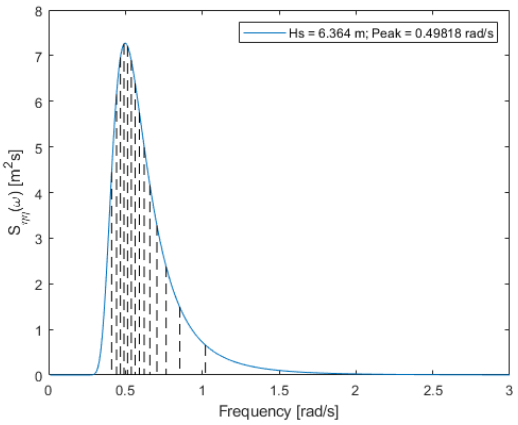

Figure 3: Pierson-Moskowitz spectrum

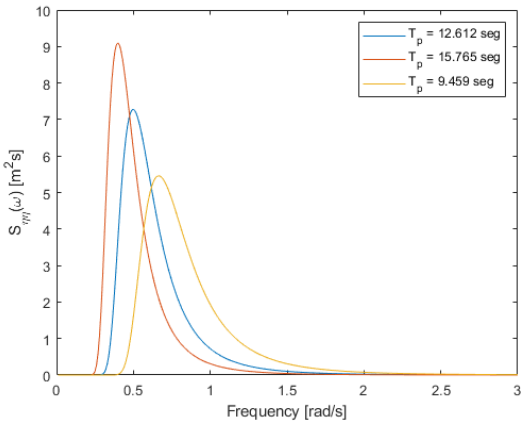

Figure 4: P-M compared with Bretschneider

Note that in the Fig. (3) and Fig. (4) the x-axis represents frequencies in rad/s while y-axis indicates the spectrum value in m^2s. In the figure from the right, the value of $T_p = 12.612$ seg is obtained using $\omega_p = 0.49818$ rad/s as the peak frequency, as calculated by Eq. (14). This represents the P-M spectrum value, where the significant wave height equals $6.364m$. The red and yellow lines correspond to the respective wave data values. The frequency segmentation in the P-M spectrum (Fig. 3 dashed lines remark) is based on a proportion of similar areas proposed by Borgman (1967). This segmentation determines the values used for wave superposition, which are obtained as follows:

$$\omega_n = \left(\frac{4 \cdot \alpha \cdot g^2 \cdot \omega_N^4}{H_s^2 \cdot \omega_N^4 \cdot \ln(N/n) + 4 \cdot \alpha \cdot g^2} \right)^{1/4} \text{for n = 1, ..., N-1.} \quad (21)$$

An analysis of an Airy wave and the respective velocities for the two wave cases and the P-M spectrum has been conducted to ascertain the influence that the change in peak period has on each wave. The results of this analysis are presented in the Fig. (5) and Fig. (6):

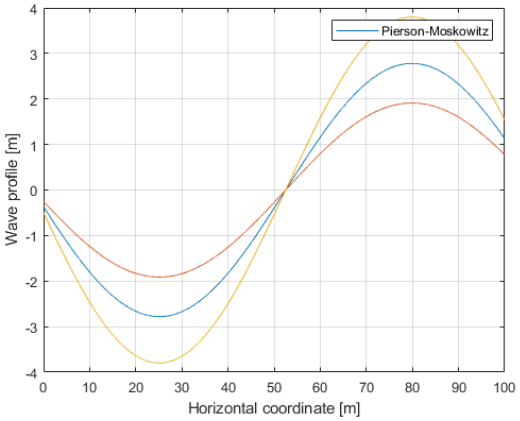

Figure 5: Airy wave profile

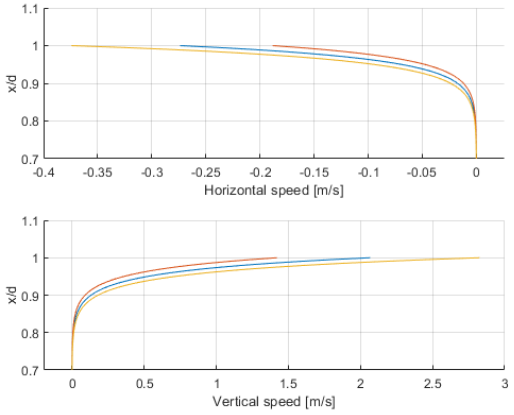

Figure 6: Horizontal and vertical speed

As indicated by Fig. (5), the horizontal coordinate in meters is represented along the x-axis, while the y-axis depicts the wave profile values, also in meters. Regarding Fig. (6) the x-axis denotes the water speed in meters per second (m/s), while the y-axis represents the dimensionless depth of the water. The lower end of the velocity range is truncated because for all cases have a value of zero. The color corresponds to the spectrum response, highlighting that as the spectrum becomes more narrow-banded, the amplitude of the wave and its corresponding speed decrease. This way, it is possible to compute a sample of irregular wave profiles and velocities using the same random phase number for all cases, with only ω_n and $\bar{k}$ being changed. The results are show in Fig. (7) and Fig. (8).

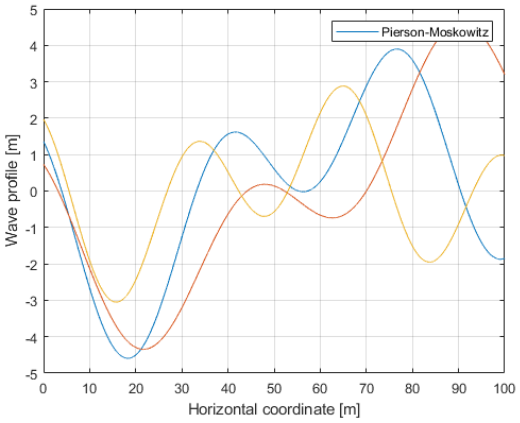

Figure 7: Irregular wave profile

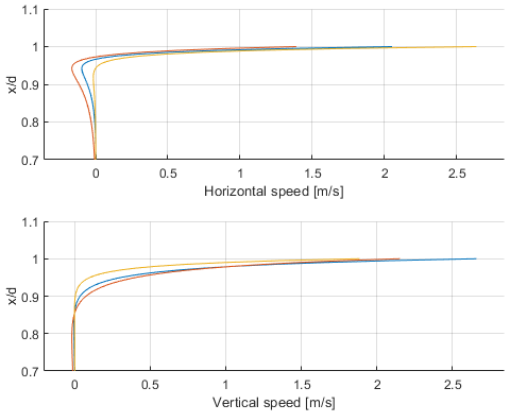

Figure 8: Irregular horizontal and vertical speed

Similarly to the Airy wave response, the motion's amplitude initially follows the expected behavior (Fig. 7). However, as the distance increases, the wave profiles become more random and unpredictable. Note that Fig. (8) exhibits a similar pattern, for the horizontal, speed to Airy wave, this is not the case for the vertical speed. The graphs depicting wave speeds illustrate the overall response of the Morison equation, assuming uniform current velocity in the flow direction. This assumption ensures that their contribution maintains the same format as the wave speed.

5. CONCLUSION

The influence of the change in T_p becomes more evident in the Airy wave. As the peak period increases, indicating a narrower spectrum, the amplitude of the wave profile decreases, along with the respective velocity. Conversely, when the T_p decreases, the wave's amplitude increases, generating a faster wave. When dealing with irregular waves, the behavior of the wave profile and speed isn't as evident due to the variation in frequencies and wave numbers. However, all the components for the superposition of waves exhibit the same behavior as seen in the Airy formulation. Therefore, it is expected that most irregular samples follow this pattern. As depicted in irregular profile, the waves exhibit a pattern at the onset of movement. As the frequencies and wave numbers begin to disassociate from each other, the behavior becomes more unpredictable. Similarly, the irregular speed presents that while the horizontal velocities adhere to the pattern shown in the Airy formulation, the vertical velocities display a different pattern. It becomes clear that choosing the correct spectrum for the ocean environment is crucial in the analysis of loads and structural responses for a multitude of offshore structures, encompassing ships, risers, cables, bridges and others. Furthermore, this enables the optimization of these structures, thereby minimizing material consumption while maintaining structural integrity.

6. REFERENCES

Bar-Avi, P. and Benaroya, H., 1997. "Stochastic response of a two dof articulated tower". *International Journal of Non-Linear Mechanics*, Vol. 32, pp. 639–655.

Benaroya, H. and Han, S.M., 2005. *Probability Models in Engineering and Science*. Taylor Francis Group, LLC, 6000 Broken Sound Parkway NW, Suite 300. 707 p.

Besedin, D., Peek, R., Ang, S.Y., Vedeld, K., Fyrileiv, O. and Gulyaev, A., 2018. "Effects of correlation between waves and currents on pipeline free span viv fatigue a case study". *Proceedings of the ASME 2018 37th International Conference on Ocean, Offshore and Arctic Engineering*, Vol. 37.

Borgman, L.E., 1967. "Ocean wave simulation for engineering design". *HYDRAULIC ENGINEERING LABORATORY, COLLEGE OF ENGINEERING*.

Fang, H. and Duan, M., 2014. *Offshore Operation Facilities*. Petroleum Industry Press, Beijing, China. 82 p.

Han, S.M. and Benaroya, H., 2000. "Non-linear coupled transverse and axial vibration of a compliant structure, part 2: Forced vibration". *Mechanical and Aerospace Engineering*, Vol. 237, pp. 875–900.

Han, S.M. and Benaroya, H., 2002. *Nonlinear and Stochastic Dynamics of Compliant Offshore Structures*. Springer-Science+Business Media, B.V., Woods Hole, MA, U.S.A. 97 p.

Hughes, O.F. and Paik, J.K., 2010. *Ship Structural Analysis and Design*. The Society of Naval Architects, Jersey City, New Jersey.

Isaacson, M., 1988. "Wave and current forces on fixed offshore structures". *Can. J. Civ. Eng*, Vol. 15, pp. 937–947.

Ishiharaa, T. and Zhang, S., 2018. "Prediction of dynamic response of semi-submersible floating offshore wind turbine using augmented morisons equation with frequency dependent hydrodynamic coefficients". *Renewable Energy*.

James, R. and Ros, M.C., 2015. "Floating offshore wind: Market technology review". *Carbon Trust*.

Journée, J. and Massie, W., 2001. *Offshore hydromechanics*. Delft University of Technology, Postbus 5,2600 AA Delft, the Netherlands, 1st edition.

Keulegan, G.H.H. and Carpenter, L.H., 1958. "Forces on cylinders and plates in an oscillating fluid". *Journal of Research of the National Bureau of Standards*, Vol. 60, pp. 423–440.

Khedkar, K., Nangia, N., Thirumalaisamy, R. and Bhalla, A.P.S., 2021. "The inertial sea wave energy converter (iswec) technology: Device-physics, multiphase modeling and simulations". *Ocean Engineering*, Vol. 229.

Mao, X., Joshi, V., Miyanawala, T. and Jaiman, R.K., 2018. "Data-driven computing with convolutional neural networks for two-phase flows: Application to wave-structure interaction". *Proceedings of the ASME 2018 37th International Conference on Ocean, Offshore and Arctic Engineering*, Vol. 37.

Mirab, H., Fathi, R., Jahangiri, V., Ettefagh, M.M. and Hassannejad, R., 2015. "Energy harvesting from sea waves with consideration of airy and jonswap theory and optimization of energy harvester parameters". *Journal of Marine Science and Application*, Vol. 14, p. 440449.

Morison, J.R., O'BRIEN, M.P., JOHNSON, J.W. and SCHAA, S.A., 1950. "The force exerted by surface waves on piles". *Petroleum Transactions, AIME*, Vol. 189, pp. 149–154.

Nizamani, Z., Nakayama, A., Uchiyama, Y. and Hai, T.K., 2019. "A review of ocean forces interaction model with offshore structures near the free surface". *AIP Conference Proceedings*, Vol. 2157. Doi: https://doi.org/10.1063/1.5126573.

Prendergast, J., Li, M. and Sheng, W., 2020. "A study on the effects of wave spectra on wave energy conversions". *IEEE Journal of Oceanic Engineering*, Vol. 41, pp. 271–283.

Sarpkaya, T.S., 2010. *Wave Forces on Offshore Structures*. Cambrige University Press, The Edinburgh Building, Cambridge CB2 8RU, UK, 1st edition. 174 p.

Silva, C.W., 2007. *Vibration Damping, Control, and Design*. Taylor Francis Group, LLC, Vancouver, Canada. Cap 11.

Sjolte, J., Sandvik, C.M., Tedeschi, E. and Molinas, M., 2013. "Exploring the potential for increased production from the wave energy converter lifesaver by reactive control". *Energies*, Vol. 6, pp. 3706–3733.

Stansby, P., Moreno, E.C. and Stallard, T., 2017. "Large capacity multi-float configurations for the wave energy converter m4 using a time-domain linear diffraction model". *Applied Ocean Research*, Vol. 68, pp. 53–64.

Wan, L., Greco, M., Lugni, C., Gao, Z. and Moan, T., 2017. "A combined wind and wave energy-converter concept in survival mode: Numerical and experimental study in regular waves with a focus on water entry and exit". *Applied Ocean Research*, Vol. 63, p. 200216.

Wilson, J.F., 2003. *Dynamics of Offshore Structures*. John Wiley Sons, Inc., Hoboken, New Jersey. 21 p.

Zauner, M., Tullio, N.D. and Sandham, N.D., 2018. "Direct numerical simulations of transonic flow around an airfoil at moderate reynolds numbers". *AIAA JOURNAL*, Vol. 57.

7. RESPONSIBILITY NOTICE

The authors are the only responsible for the printed material included in this paper.